Journal of Materials Chemistry B

ROYAL SOCIETY OF CHEMISTRY

PAPER

View Article Online
View Journal | View Issue

Cite this: J. Mater. Chem. B, 2026, 14, 4755

Photothermally triggered silk fibroin microneedles with coordinated gallic acid–iron networks for synergistic infected burn wound therapy

Wang Sun,†[ab] Rui Xu,†[a] Wenshuya Li,†[c] Ziyan Chen,[a] Mengting Yin,[d] Haibo Liu,[d] Feng Chen,*[abd] Haijian Ni*[a] and Xinyu Zhao*[a]

Infected burn wounds remain a formidable clinical challenge due to persistent oxidative stress, bacterial infection, and dysregulated inflammation. Herein, a multifunctional microneedle (MN) patch is engineered through the *in situ* integration of gallic acid–iron coordination networks (GFe) onto silk fibroin microspheres (SFMSs). The resulting GFe@SFMSs are encapsulated into a dissolvable MN array, enabling direct intradermal delivery and sequential therapeutic release. Leveraging the relatively weak nature of the coordination bonds, this composite structure exhibits photothermal antibacterial activity (>99% inhibition against *E. coli* and *S. aureus*) during the early stage of wound healing, and then gradually degrades in the subsequent phase to release iron ions and gallic acid, conferring durable antioxidant, anti-inflammatory, and chemodynamic effects. Simultaneously, the progressive degradation of SFMSs can activate endogenous regenerative pathways, thereby promoting collagen synthesis and angiogenesis. In a murine infected burn model, the MN patch significantly accelerates wound closure, reduces pro-inflammatory cytokines (TNF-α, IL-6), and enhances tissue remodeling. This work presents a synergistic and spatiotemporally programmable strategy for infected burn healing through the combination of photothermal, chemodynamic, antioxidant, and regenerative functions.

Received 19th January 2026,
Accepted 24th March 2026

DOI: 10.1039/d6tb00149a

rsc.li/materials-b

1. Introduction

Burn injuries represent a critical global health challenge, with over 9 million cases requiring medical attention each year and an associated annual mortality of approximately 180 000.[1] The clinical management of burn wounds is severely complicated by a persistent, reactive oxygen species (ROS)-driven inflammatory microenvironment, which compromises the efficacy of conventional dressings.[2] This dysregulation triggers a vicious cycle wherein ROS perpetuate inflammation, trapping the wound in a non-healing state, suppressing proliferation, and elevating risks of infection, sepsis, and mortality.[3–5] Consequently, there is an urgent, unmet need for advanced dressings capable of simultaneously quenching ROS, modulating immune responses, and eradicating pathogens to restore the healing cascade.

Silk fibroin (SF), a natural protein polymer, has garnered significant interest as a regenerative biomaterial due to its outstanding biocompatibility, tunable biodegradability, and favorable mechanical properties.[6–8] Studies demonstrate that SF actively orchestrates wound repair by promoting neovascularization and polarizing macrophages toward a pro-regenerative M2 phenotype during inflammation,[9] and by activating the NF-κB pathway to upregulate VEGF and TGF-β1 during proliferation, thereby enhancing granulation tissue formation and collagen deposition.[10–12] These attributes position SF as an ideal base material for burn wound dressings.[13] However, its inherent lack of antibacterial activity severely limits its utility in infected wounds, a common and life-threatening complication.[14,15] Thus, endowing SF-based dressings with potent, long-lasting antimicrobial functionality without compromising their regenerative performance remains a pivotal challenge for clinical translation.[15,16]

Polyphenolic molecules, such as gallic acid (GA), present a compelling solution by integrating broad-spectrum antibacterial efficacy with inherent antioxidant and anti-inflammatory activities.[17] Moreover, these molecules can coordinate with

[a] Center for Orthopaedic Science and Translational Medicine, Department of Orthopaedics, Shanghai Tenth People's Hospital, School of Medicine, Tongji University, Shanghai, 200072, P. R. China. E-mail: xyzhao@tongji.edu.cn, nihaijianch@163.com, chen_feng@fudan.edu.cn
[b] Suzhou First People's Hospital, School of Medicine, Anhui University of Science and Technology, Anhui, 234000, P. R. China
[c] Department of Plastic Surgery, The Second Hospital of Hebei Medical University, Shijiazhuang, Hebei, P. R. China
[d] Shanghai Key Laboratory of Craniomaxillofacial Development and Diseases, Shanghai Stomatological Hospital & School of Stomatology, Fudan University, Shanghai, P. R. China
† Authors contributed equally.

metal ions to form stable, monodisperse coordination complexes. Such metal–phenolic networks (MPNs) not only deliver bioactive metal ions but also confer efficient photothermal conversion capability under near-infrared (NIR) light, enabling localized hyperthermia.[18–20] This combination yields a powerful synergistic antibacterial effect, merging physical (photothermal) and chemical (polyphenol/metal ion) modes of action.[21–24] Critically, the coordination bonds are stable under physiological conditions yet undergo controlled dissociation in the wound milieu, allowing sustained release of bioactive components and offering a versatile platform for surface engineering.[25,26]

Photothermal therapy (PTT) is a promising non-invasive strategy for infected burn wounds, with rapid and broad-spectrum antibacterial effects. It uses photothermal agents to convert near-infrared (NIR) light into local heat (50–60 °C) to ablate bacteria, and recent advances focus on developing agents like metal nanoparticles, carbon-based materials, and metal–phenolic networks (MPNs).[27,28] Current PTT platforms face critical limitations: metal nanoparticle-based systems often provoke undesirable inflammatory responses yet lack tissue regenerative capabilities, while carbon-based photothermal agents suffer from poor biocompatibility and biodegradability, collectively hindering clinical translation.[29]

Microneedle (MN) technology has emerged as a promising minimally invasive platform for the therapy of infected burn wounds, a formidable clinical challenge characterized by persistent oxidative stress, bacterial infection, and dysregulated inflammation. Recent advances have focused on integrating MNs with natural biomaterials and functional coordination networks to synergistically address these barriers and facilitate tissue regeneration.[30–33] Such dissolvable MN systems can achieve direct intradermal delivery through burn eschar, realizing sequential antibacterial activity, sustained release of bioactive components, and effective regulation of the wound microenvironment. By synergizing multiple therapeutic functions to scavenge reactive oxygen species, modulate inflammatory responses, and promote collagen synthesis and angiogenesis, these MN-based strategies overcome the limitations of traditional dressings, providing a versatile and biosafe approach for tissue regeneration in infected burn wound management.

Herein, we design a multifunctional microneedle (MN) patch for synergistic therapy of infected burn wounds (Fig. 1). We construct a photothermally active nanocoating on silk fibroin microspheres (SFMSs) *via* an *in situ* coordination between Fe^{3+} and GA, generating gallic acid iron-decorated SFMSs (GFe@SFMSs). These functional microspheres are then integrated into a dissolvable microneedle array fabricated from silk fibroin (tips) and γ-polyglutamic acid (base) – an FDA-recognized, highly biocompatible polymer ideal for transdermal delivery.[34,35] The resulting GFS-MN patch operates through a staged, multi-mechanistic strategy: (i) upon application, the MN penetrates the burn eschar, ensuring direct intradermal delivery; (ii) initial NIR irradiation triggers rapid photothermal

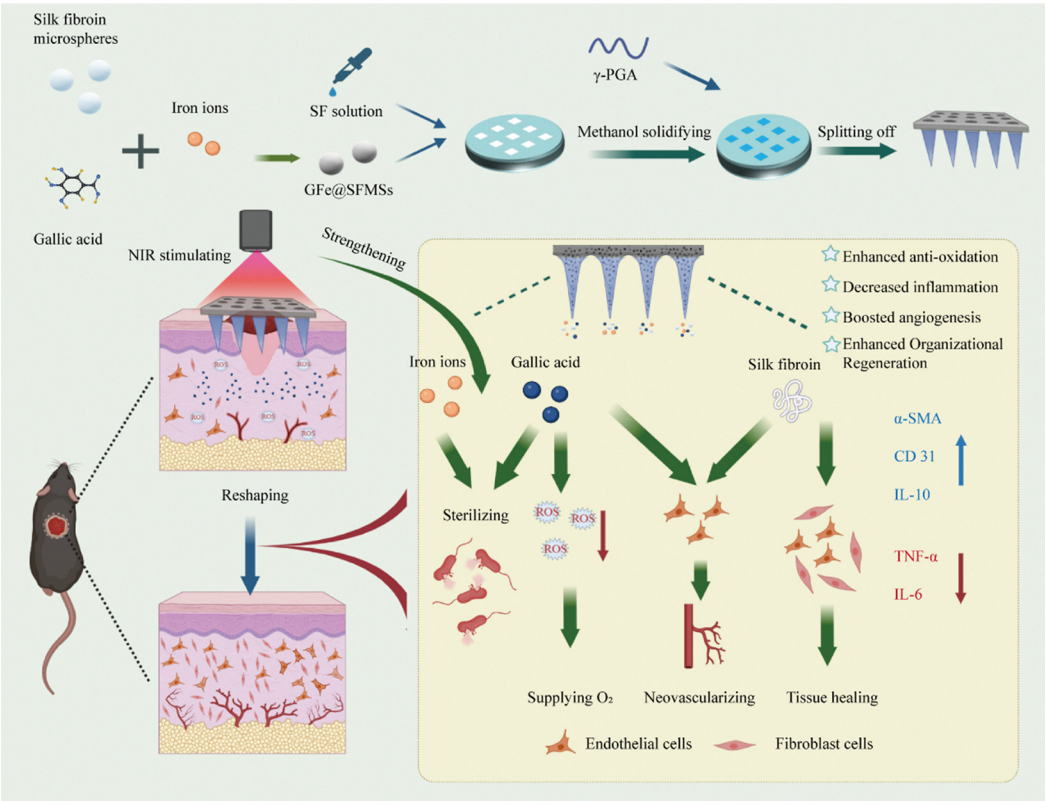

Fig. 1 Schematic illustration of the design and fabrication of the GFe@SFMSs integrated microneedle (GFS-MN) patch for infected burn wound healing.

sterilization *via* the GFe coating; (iii) subsequent gradual dissociation of the Fe–GA network in the wound bed enables sustained release of GA (exerting antibacterial, antioxidant, and anti-inflammatory effects) and Fe ions (participating in chemodynamic reactions); (iv) concurrently, the degraded SFMSs activate endogenous regenerative pathways, including NF-κB, to promote collagen synthesis and tissue remodeling.[11,15,36,37] This design uniquely converges on-demand photothermal ablation with long-lasting chemodynamic/antioxidant therapy and innate immunomodulation. We demonstrate that this synergistic platform significantly accelerates the healing of infected burn wounds by simultaneously eradicating pathogens, scavenging ROS, modulating inflammation, and enhancing regeneration, offering a promising and innovative strategy for advanced wound care.

2. Experimental section

2.1. Materials

Polyvinyl alcohol ($[–CH_2–CH(OH)–]_n$) was purchased from Shanghai Chenqi Chemical Technology Co., Ltd. Glutaraldehyde ($C_5H_8O_2$), ferric nitrate nonahydrate ($Fe(NO_3)_3{\cdot}9H_2O$), NaOH, absolute ethanol, 2,2-diphenyl-1-picrylhydrazyl (DPPH), and ethylbenzthiazoline-6-sulfonic acid (ABTS) were obtained from Aladdin Industrial Corporation, Shanghai, China. Silk fibroin was acquired from Suzhou Pinglan Biotechnology Co., Ltd. 3,3′,5,5′-tetramethylbenzidine (TMB) was sourced from Shanghai Macklin Biochemical Co., Ltd., Shanghai, China. Bacterial strains used in this study included the Gram – positive *Staphylococcus aureus* (*S. aureus*) (ATCC 6538), obtained from Haibo Biotech Company, Qingdao, China, and *Escherichia coli* (ATCC 8739), procured from Shanghai Fuxiang Biotechnology Co., Ltd., Shanghai, China. Cell viability and cell death assay kits, as well as the CCK – 8 assay kit, were sourced from Beyotime Biotechnology, Shanghai, China. Dulbecco's Modified Eagle Medium (DMEM) and Trypsin – EDTA were obtained from Thermo Fisher Scientific, Wilmington, Massachusetts, USA. All solutions were prepared using deionized water and freshly prepared for each experimental session to ensure optimal reactivity. All chemicals used in this study were of reagent – grade quality and were used without further purification, as received from the manufacturers.

2.2. Preparation of SFMSs and GFe@SFMSs

The synthesis method was referenced from our previous work.[38] In brief, SFMSs were first synthesized *via* PVA-induced β-sheet formation. Subsequently, 100 mg of SFMSs were added to a mixture containing 4 mg mL^{-1} GA and 3 mg mL^{-1} $Fe(NO_3)_3{\cdot}9H_2O$. Then, NaOH was added to adjust the acidity of the solution to a weak level. After a 24 – hour reaction, the mixture was purified three times with deionized water and stored at 4 °C for further use.

2.3. Preparation of GFS-MN

Preparation of GFS-MN: the microneedle mold was fabricated using the electric discharge machining process (Micropoint Technologies Pet. Ltd., Singapore). The microneedle array consists of a 10 × 10 matrix, with each microneedle tip measuring 200 × 200 × 500 μm (width × length × height). A 10% (w/v) SF solution was prepared, and GFe@SFMSs were incorporated into the SF solution to achieve a final concentration of 4 mg mL^{-1} GFe@SFMSs. This mixture was then applied to the microneedle tips using a vacuum infiltration method. Excess SF solution was removed, and the microneedles were placed in a vacuum chamber containing methanol vapor at 60 °C to promote SF β – sheet formation, thereby enhancing the mechanical properties of the microneedle tips. Finally, a solution containing 4 mg mL^{-1} GFe@SFMSs and 0.32 g mL^{-1} γ- PGA was applied to the microneedles to form a soluble base layer. Blank microneedles without GFe@SFMSs were prepared using the same method.

2.4. Materials characterization

The microstructure of the samples was characterized using a field – emission scanning electron microscope (SEM, Hitachi S – 4800, Japan). Elemental composition was analyzed using an energy – dispersive spectrometer (EDS, Gemini S – 300, Zeiss, Germany) and an X – ray photoelectron spectrometer (XPS, Thermo Scientific K – Alpha, USA). Powder X – ray diffraction (XRD) patterns were collected on a SmartLab 9kW diffractometer from Rigaku Corporation, Japan, using Cu Kα radiation (wavelength = 1.5406 Å) at a scanning rate of 5° per minute. Fourier – transform infrared (FTIR) spectra were acquired on an FTIR spectrometer (Nicolet iS10, Thermo Scientific, USA) over the wavenumber range of 4000 to 400 cm^{-1}, with 32 scans for each sample at a resolution of 4 cm^{-1}. Ultraviolet – visible absorption spectra were obtained using a UV – Vis spectrophotometer (Evolution UV201, Thermo Fisher Scientific, USA). The particle sizes of SFMSs and GFe@SFMSs were calculated using ImageJ software.

2.5. Assessment of antioxidant activity of GFe@SFMSs

UV–vis spectroscopy was employed to monitor and assess the antioxidant activity of samples using commonly utilized assays, such as the DPPH assay and the ABTS assay. For the DPPH assay, prepare a pre – made solution of 125 μM DPPH in ethanol. Then, mix it in equal volumes with different concentrations of GFe@SFMSs (0, 50, 100, and 200 μg mL^{-1}), and co – incubate the mixture in the dark for 30 min. Finally, measure the absorbance at 519 nm using UV–vis spectroscopy. For the ABTS assay, prepare a 7 mM solution of ABTS. Incubate it overnight with a 2.45 mM potassium persulfate solution to activate ABTS radicals. Subsequently, mix 0.6 mL of different concentrations of GFe@SFMSs with 2.4 mL of the ABTS solution for 10 min. Finally, measure the absorbance at 734 nm by ultraviolet – visible spectroscopy.

2.6. *In vitro* antibacterial property

The antibacterial performance of GFe@SFMSs against *S. aureus* (ATCC 6538) and *E. coli* (ATCC 8739) was evaluated using the plate – counting method. After co – culturing the bacterial suspension with GFe@SFMSs at varying material concentrations for 4 h, the bacterial suspension was diluted and spread on agar plates. These plates were then incubated at 37 °C for

24 h to count the number of colonies. The GFS-MN and MN were exposed to UV light for 12 h. *S. aureus* and *E. coli* were used to evaluate the antibacterial characteristics of different groups under NIR and non – NIR conditions. The bacterial suspensions (1.0×10^9 CFU mL^{-1}) were cultured with different groups. The GFS-MN + NIR group was irradiated to reach 50 ± 0.5 °C for 6 min with a NIR laser (1.0 W cm^{-2}). The MN and GFS-MN groups were not irradiated. Bacteria without treatment were taken as the blank control. After incubation at 37 °C for 4 h, the antibacterial property was assessed by the plate – counting method. Then, using physiological saline as the solvent, the bacterial culture was co – incubated with the material. After that, it was fixed using a 2.5% glutaraldehyde solution and dehydrated incrementally with ethanol solutions at 20%, 40%, 60%, 80%, and 100% concentrations. Subsequently, the morphological alterations of the bacterial membrane were examined under a scanning electron microscope.

2.7. *In vitro* load iron and release iron

To assess the release profile of Fe, GFe@SFMSs (5 mg) were immersed in PBS (5 mL, 0.1 M, without calcium and magnesium, pH 7.4) and kept in a 37 °C incubator shaker. At each predetermined time point (1, 3, 6, 12 and 24 hours, and 3, 7 and 14 days), 4 mL of the sample liquid was collected and replaced with an equal amount of fresh PBS. Inductively coupled plasma optical emission spectrometry (Agilent 720ES, USA) was employed to analyze the Fe concentration.

2.8. Assessment of photothermal performance

Firstly, the photothermal performance of GFe@SFMSs was systematically evaluated by monitoring the temperature elevation of aqueous dispersions (0.25–16 mg mL^{-1}) under continuous NIR irradiation (808 nm, 1.0 W cm^{-2}, 10 min). Subsequently, a 4 mg mL^{-1} suspension was exposed to incremental laser power densities (0.5, 1.0, 1.5, and 2.0 W cm^{-2}) for approximately 10 min, and the corresponding temperature profiles were recorded. An identical power – density series (0.5–2.0 W cm^{-2}, approximately 6 min each) was applied to the GFS-MN patch to assess its power – dependent photothermal response. Surface – temperature mapping of blank MN and GFS-MN under NIR illumination (1.0 W cm^{-2}, 6 min) was acquired in real time using an infrared thermal camera. Finally, the photothermal stability of GFS-MN was examined over four consecutive ON/OFF laser cycles (1.0 W cm^{-2}, 6 min per cycle).

2.9. Assessment of the *in vitro* sustained-release capability of MN

For the assessment of the sustained – release capability of MN, rhodamine B was used as a substitute for GFe@SFMSs and loaded into the microneedles. Microneedles with rhodamine B – loaded tips were prepared at a rhodamine B concentration of 1 mg mL^{-1}. Four microneedle patches were immersed in 4 mL of PBS buffer solution. At seven time points ranging from 0.04 to 7 days, 3 mL of the solution was sampled and replaced with an equal volume of fresh PBS buffer. The concentration of rhodamine B in the solution was then measured by detecting the UV absorption peak at 554 nm. Subsequently, based on the calibration curve extracted from Fig. S3 (SI), the concentration of rhodamine B in the supernatant was calculated from the absorbance values:

$$\text{Release (\%)} = C_m/M_0 \times 100\% \quad (1)$$

where C_m referred to the calculated concentration of rhodamine B in the supernatant at m min and M_0 refers to the mass of rhodamine B loaded to the GFS-MN.

2.10. Transdermal experiment of MN

For the transdermal experiment of microneedles (MN), the MN were inserted into the skin of BALB/c mice. Subsequently, the skin tissues were further fixed in 4% paraformaldehyde and stained with hematoxylin and eosin (H&E). Then, the transdermal results were observed.

2.11. Cell culture—*in vitro* evaluation of cell toxicity and functional assays

The biocompatibility of GFe@SFMSs: Initially, the non – cytotoxic concentrations of GFe@SFMSs for cell culture experiments were determined using the Cell Counting Kit – 8 (CCK – 8). In brief, NIH/3T3 cells were seeded in 96 – well plates at a density of 10 000 cells per well and allowed to grow without treatment. Then, the cells were incubated with a range of eight different concentrations of GFe@SFMSs (0–800 μg mL^{-1}). In accordance with the manufacturer's instructions for the CCK – 8 kit (Beyotime, China), 100 μL of serum – free culture medium and 10 μL of CCK – 8 solution were added to each well and incubated for 2 h at 37 °C in a CO_2 incubator. Absorbance at 450 nm was subsequently measured using a microplate reader (Thermo Fisher, USA). For each sample, six replicate wells were established. The toxicity of each group of MNs was determined using the same method. Live/Dead Cell Assay: in this assay, 5×10^4 NIH/3T3 cells were seeded per well in a 24 – well plate and cultured overnight. Then, the cells were allocated to different groups and cultured for an additional 24 h, with an equal volume of complete DMEM medium serving as a blank control. The supernatant was collected, and the NIH/3T3 cells were washed three times with PBS. Subsequently, 150 μL of staining solution was added to each well, following the protocol outlined in the live/dead cell assay kit (Beyotime, China). After the staining solution was removed, cellular imaging was conducted using a fluorescence microscope (Eclipse TS2R, Nikon Corporation, Japan). Each experimental group included at least three replicates, with multiple repetitions to ensure data reliability.

In vitro proliferation experiments: HUVEC and NIH/3T3 cells were seeded in 96 – well plates at 5×10^3 cells per well. Then, 100 μL of microneedling solution was added to each well to detect cell proliferation at 1, 2, and 3 respectively. Subsequently, the absorbance at 450 nm was measured using a microplate reader (Thermo Fisher, USA). Cell viability was calculated by the following equation:

$$\text{Cell viability (\%)} = [(\text{ODs} - \text{ODb})/(\text{ODn} - \text{ODb})] \times 100 \quad (2)$$

where ODs was the OD value of the well with cells, extracts, and CCK-8, ODb was the OD value of the well with medium and CCK-8, and ODn was the OD value of the well with cells, media, and CCK-8. Cell Culture—Hemolysis Ratio Test: fresh blood was collected from the carotid artery of SD rats using an anticoagulant tube. Then, a 4% w/v erythrocyte solution was obtained by centrifuging the heart blood at 1500 rpm for 15 min and resuspending the pellet with PBS. Different MN suspensions prepared previously were used as experimental groups. 500 μL of each suspension was aspirated and added to a 1.5 mL centrifuge tube. 500 μL of deionized water and PBS were set as positive and negative controls, respectively. A solution with a final concentration of 2% w/v was prepared by adding 500 μL of erythrocyte suspension to each tube. After further incubation at 37 °C for 4 h, the samples were centrifuged at 1500 rpm for 15 min. 100 μL of the supernatant was aspirated and transferred to a 96 – well plate, and the 96 – well plate was placed in the studio for taking pictures. Finally, absorbance values at 540 nm were measured using a microplate reader (SpectraMax iD5, Molecular Devices, CA, USA) to assess hemoglobin release. Data were presented as the mean with standard deviation (mean ± SD, $n = 6$). The hemolysis ratio was calculated using the following equation:

$$\text{Hemolysis ratio (\%)} = [(A_{bss} - A_{bsn})/(A_{bsp} - A_{bsn})] \times 100\% \quad (3)$$

where A_{bss}, A_{bsn}, and A_{bsp} were the absorbance values of experimental, negative control, and positive control groups, respectively

Cell Culture—Cell Migration Assay: HUVEC and NIH/3T3 cells were plated in a six – well plate at 1×10^5 per well. The cells were grown to 100% confluence. A clear area was created using a 200 μL pipette tip from the top to the bottom of the well. The microneedle solution was prepared with DMEM medium containing 1% FBS. Add 2 mL of the microneedle suspension to each well and record the size of the cell migration area using phase – contrast microscopy at 0 and 24 h. Each tablet of microneedles was dissolved in 4 mL of DMEM medium containing 10% FBS to prepare the microneedle suspension.

$$\text{Healed wound area (\%)} = (A_0 - A_{24})/A_0 \times 100\%. \quad (4)$$

where A_0 represents the initial wound area, and A_{24} represents the residual wound area.

Using a transwell-dedicated 24-well plate, add FBS-free medium resuspended NIH/3T3 cells to the upper chamber at a ratio of 2×10^4 cells per well. In a 24 – well plate, different microneedle suspensions were placed under the chamber containing 10% FBS to enable the free exchange of fluid and nutrients between the upper and lower chambers. After 24 h of incubation, use a cotton swab to remove non – migrating cells and fix the migrating cells with paraformaldehyde. Finally, stain with crystal violet, perform light field photography, and conduct counting.

Cell Culture—Determination of Intracellular ROS Levels: DCFH – DA staining was employed to analyze the intracellular ROS clearance capacity. Typically, NIH/3T3 cells were incubated at a density of 1×10^4 cells per well in a 24 – well plate for 12 h. Subsequently, different microneedle solutions were added, allowing the cells to grow to 80% confluence. Then, the cells were treated with H_2O_2 at a concentration of 100 μM for 45 min. After that, the cells were washed three times with PBS and incubated with DCFH – DA (10 μM) for 30 min at 37 °C in the dark. The cells were observed under a fluorescence microscope (Ts2R – FL, Nikon, Tokyo, Japan).

2.12. *In vivo* wound healing

2.12.1. Burn infected wound model. All surgical protocols conformed to the NIH Guide for the Care and Use of Laboratory Animals and were approved by the Animal Ethics Committee of Shanghai Tenth People's Hospital, Tongji University School of Medicine (approval No. SHDSYY – 2024 – SW2180). Twenty – four BALB/c mice (8 weeks old) were randomly assigned to four groups ($n = 6$ per group). A reproducible burn – infection model was generated as previously described.[39] After isoflurane anaesthesia, the dorsal fur was shaved, and a deep – partial – thickness burn was created by applying a 10 – mm copper disc pre – heated to 90 °C to the exposed skin for 15 s. Twenty – four hours later, the necrotic eschar was excised, and 100 μL of *Staphylococcus aureus* suspension (1×10^8 CFU mL^{-1}) was evenly inoculated onto the wound bed. Purulent exudate was evident within 12 h, confirming infection. Mice then received a single application of photothermal GFS-MN, non – photothermal GFS-MN, or blank microneedles (MN); untreated animals served as the blank control. Wound evolution was documented with a digital camera on days 0, 3, 7, 10, and 14. The exposed area was quantified with ImageJ (NIH, Bethesda, MD, USA), and percentage wound closure was calculated as:

$$\text{(area of original wound} - \text{area of actual wound)/area of original wound} \times 100\%. \quad (5)$$

On the 7th day after treatment, a batch of mice were sacrificed to obtain wound tissues for ROS (Reactive Oxygen Species) staining. The intensity of immunofluorescence was then calculated using ImageJ software.

2.13. Histological evaluation and immunofluorescence staining

On day 14, the animals were euthanized. The wounds, along with the adjacent normal skin and major organs (heart, lungs, liver, spleen, and kidneys), were excised, fixed in 4% paraformaldehyde, and processed for subsequent histological and immunohistochemical evaluation. After dehydration and paraffin embedding, 5 μm sections were cut and mounted on glass slides. The skin sections were stained with hematoxylin–eosin (H&E; Runbio, Shanghai, China) and Masson's trichrome (Runbio) according to the manufacturers' protocols. To evaluate the inflammation and angiogenesis of the wounds, immunofluorescence was used to detect the expression of CD31, α-SMA, IL-6, IL-10, and TGF-α in the wound tissue. The skin tissue was fixed with 4% phosphate-buffered paraformaldehyde

and embedded in paraffin. The sections were subjected to immunofluorescence staining for CD31, α-SMA, IL-6, IL-10, and TGF-α. The stained sections were observed using an optical microscope (Leica, Wetzlar).

3. Results and discussion

3.1. Preparation of SFMSs and GFe@SFMSs

The SFMSs were synthesized using the PVA-induced β-sheet method. Initially, PVA-stabilized microemulsions containing silk fibroin were formed by applying mechanical shear forces to the solution. Subsequently, during the drying phase, the evaporation of the solvent inhibited droplet coalescence and facilitated the solidification of the PVA–SF composite film. Finally, the dried film was processed through dissolution and centrifugation steps to obtain silk fibroin microspheres (SFMSs). Scanning electron microscopy (SEM) analysis revealed that SFMSs primarily exhibited spherical or ellipsoidal shapes with an average diameter of 4.26 ± 0.91 μm (Fig. 2a, b and f). The GFe@SFMSs were prepared by an *in situ* surface modification method using a coordination reaction between Fe^{3+} and GA. Gallic acid (GA) contains three hydroxyl groups and one carboxyl group, which can chelate with Fe^{3+} to form stable coordination bonds (Fe^{3+}–O–R, where R is the aromatic ring of GA). Additionally, the hydroxyl groups of GA can form hydrogen

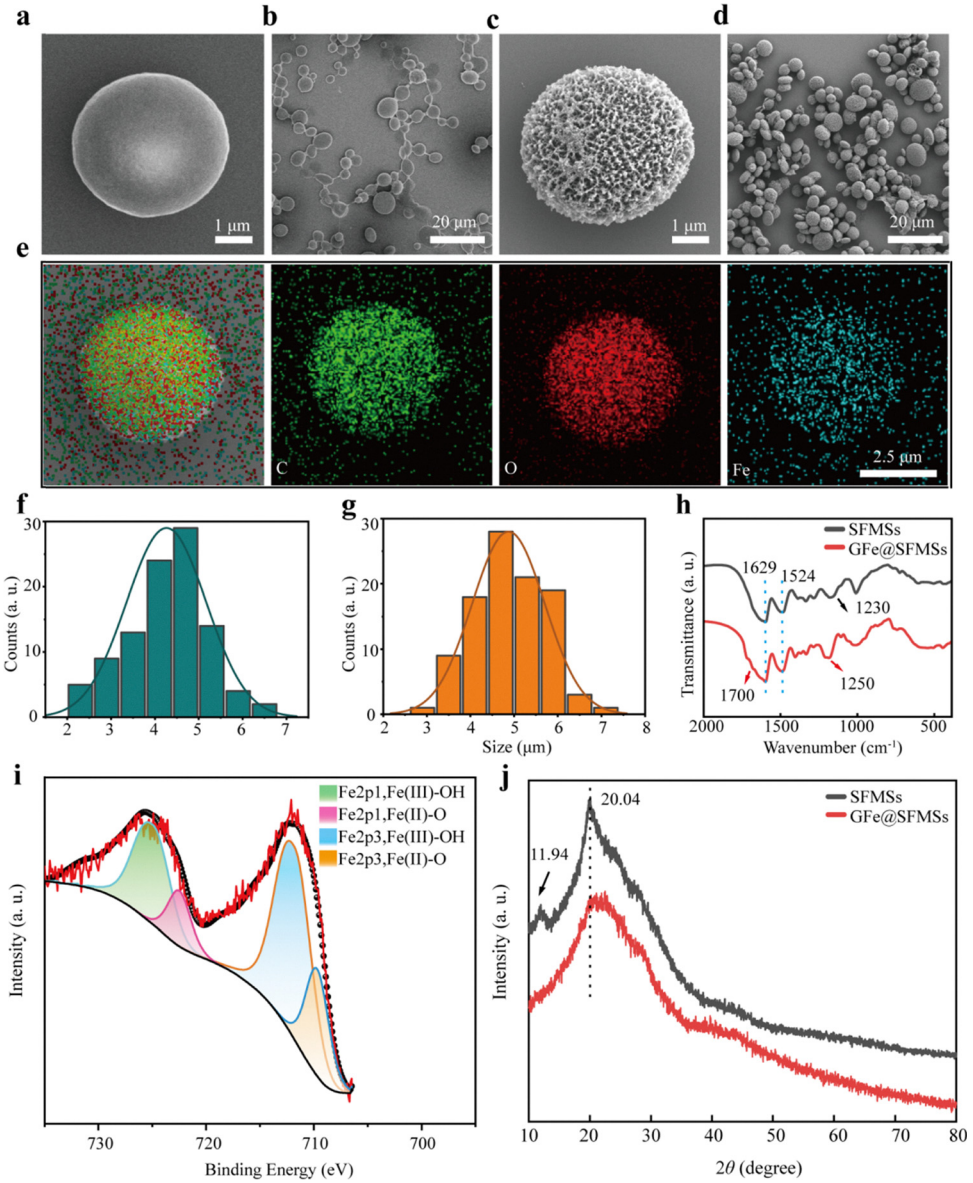

Fig. 2 Characterization of the SFMSs and GFe@SFMSs: (a) and (b) SEM images of SFMSs (Scale bars: 1 μm and 20 μm). (c) and (d) SEM images of GFe@SFMSs (Scale bars: 1 μm and 20 μm). (e) EDS analysis of O, C, and Fe elements in the GFe@SFMSs (Scale bars: 2.5 μm). (f) and (g) Particle size distribution of SFMSs (f) and GFe@SFMSs (g). (h) FTIR spectra of SFMSs and GFe@SFMSs. (i) XPS spectrum of GFe@SFMSs. (j) XRD patterns of SFMSs and GFe@SFMSs.

bonds with the amide groups (–CONH–) of SFMSs, which enables the uniform and stable *in situ* deposition of GFe network on the surface of SFMSs. This dual interaction (coordination bonding and hydrogen bonding) ensures the structural stability of GFe@SFMSs. GFe@SFMSs exhibited a uniform spherical-to-ellipsoidal geometry densely armored on the GFe NPs, presenting an average diameter of 4.87 ± 0.83 μm (Fig. 2c, d and g). Based on the particle size difference before and after modification, the thickness of the uniformly coated GFe coordination network on the SFMS surface was calculated to be 0.305 ± 0.04 μm. Energy-dispersive spectroscopy (EDS) mapping revealed a homogeneous iron signal across the entire microsphere surface and cross-section, confirming the uniform deposition of GFe NPs (Fig. 2e).

Fourier-transform infrared (FTIR) spectroscopy confirmed the formation of Fe^{3+}–gallate coordination (Fig. 2h). After *in situ* deposition of GFe NPs, the C–O stretching vibration of SFMSs at 1230 cm^{-1} shifted to 1250 cm^{-1},[40] while a new shoulder emerged at 1325 cm^{-1} attributable to ν(C–O–Fe) of the phenolate complex. These spectral changes, together with the attenuation of the 1700 cm^{-1} carbonyl band of free GA, evidenced chelation between Fe^{3+} and the gallate pyrogallol moiety on the microsphere surface. The XPS spectra show the coexistence of all the compositional elements, including Fe, O, and C elements, further confirming the successful loading of Fe on GFe@SFMSs (Fig. S1, SI). The deconvoluted spectrum for the Fe 2p peaks located at 710.7 and 724.3 eV presents two doublets, demonstrating a main valence state of Fe^{2+} together with Fe^{3+} (Fig. 2i). The dominant peaks at 709.69 eV and 722.49 eV can be assigned to the 2p3/2 and 2p1/2 in the Fe 2p spectrum of Fe^{2+}, indicating that some Fe^{3+} ions have been reduced to Fe^{2+} ions by GA. Partial reduction of Fe^{3+} ions to Fe^{2+} ions is due to the reducing environment provided by gallic acid molecules. X-ray diffraction (XRD) analysis revealed distinct crystalline peaks for SFMSs at 11.94° and 20.04°, confirming their successful synthesis. In contrast, GFe@SFMSs exhibited a hump at approximately 20.04°, indicating the formation of an amorphous phase due to the incorporation of GFe NPs (Fig. 2j).

The inherent weak interaction characteristics of the coordination bonds between Fe^{3+} and GA facilitated the release of Fe^{3+} ions from GFe@SFMSs under physiological salt conditions. The release of Fe^{3+} ions increased rapidly within the first 24 h and reached a plateau at 72 h (Fig. S2, SI). The liberated Fe^{3+} not only replenishes the iron-deficient wound milieu but also drives a localized Fenton reaction, amplifying ROS-mediated bacterial killing while remaining below systemic toxicity thresholds.

3.2. Synthesis and characterization of GFS-MN

Silk fibroin (SF) is characterized by exceptional tensile strength and a high Young's modulus, which can be significantly enhanced through β-sheet crystallization. This process promotes the formation of physically crosslinked β-sheet structures, significantly improving the mechanical robustness and structural stability of SF-based materials. Consequently, SF was chosen as the structural material for the microneedle (MN) tips to ensure effective and reliable penetration into indurated burn eschar. γ-Poly-glutamic acid (γ-PGA) was employed as the water-soluble matrix to take advantage of its characteristic of rapid erosion in a humid physiological environment.

The GFe@SFMSs integrated microneedle (GFS-MN) patches were fabricated using a two-step solvent-casting protocol with a 10 × 10 needle array polydimethylsiloxane (PDMS) female mold to produce uniform microneedle patches (Fig. 3a and b). Optical and SEM images revealed that the MN patches had a uniform conical needle tip array with a height of 500 ± 12 μm and a base diameter of 200 ± 8 μm (aspect ratio 2.5 : 1, Fig. 3c). EDS mapping results confirmed the uniform distribution of Fe, O, and C elements in the GFS-MN (Fig. 3d), indicating that GFe@SFMSs were uniformly encapsulated within each MN for subsequent burn-wound therapy.

To investigate the release kinetics of the cargo (*e.g.*, GFe@SFMSs) from the microneedles (MNs), MN patches loaded with rhodamine B (a commonly used model drug for tracking release behavior) were incubated in phosphate buffered saline (PBS, pH 7.4). The absorbance of the supernatant was measured spectrophotometrically at 554 nm—the characteristic absorption wavelength of rhodamine B—at predetermined time intervals to quantify the amount of rhodamine B released. The content of released rhodamine B was calculated according to the standard curve shown in Fig. S3, which was used to characterize the drug release capability of the MNs. The results indicated that more than 80% of the loaded drug was released within the first day, followed by a continued and gradual release over the subsequent two days (Fig. S4, SI). This sustained release profile demonstrates the effective drug retention and controlled release capability of the MNs. Mechanical properties are crucial for MNs to penetrate skin tissue and accurately deliver drugs or NPs to deeper tissues. A compression test was performed on the GFS-MN patches using a pressure testing instrument, during which the application force on the GFS-MN patch was monitored as a function of time. The results show that GFS-MN can withstand a compression force of more than 0.74 N/needle (Fig. 3e). This value is significantly higher than the critical force required for a single MN to successfully penetrate burned skin tissue (~0.5 N), indicating that GFS-MN have sufficient mechanical strength and penetration capability to effectively deliver drugs transdermally through burned skin tissue. In the subsequent histological studies, the penetration performance of MNs in burn wounds was evaluated. Sharp conical channels can be observed within the epidermal layer of the burn wound upon application of MNs. This morphological observation indicates that the tips of the MNs can effectively penetrate the epidermal layer of the burn wound, as shown in Fig. 3f. Therefore, the application of MNs is minimally invasive and can successfully penetrate the epidermal barrier of the burn wound. This penetration capability allows drugs to be directly delivered to the basal layer cells and adjacent connective tissues of the burn wound, effectively bypassing the physiological barrier of the epidermis and providing an efficient and precise pathway for drug delivery to burn wounds.

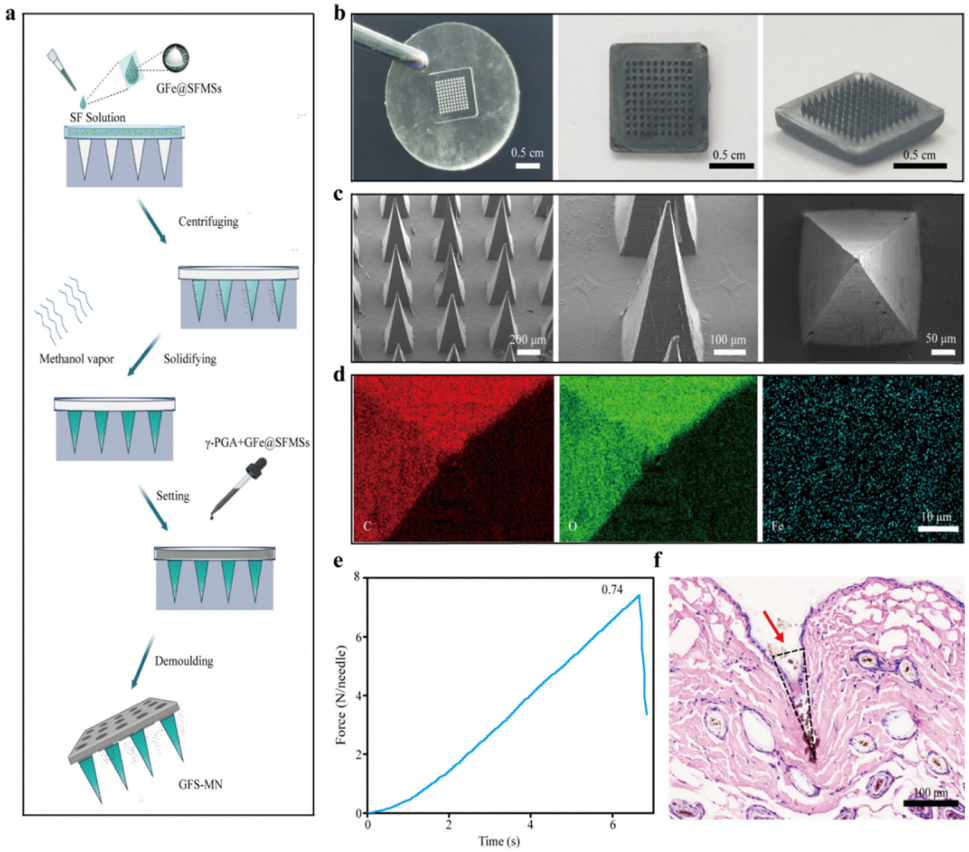

Fig. 3 Synthesis and characterization of GFS-MN: (a) schematic illustration of the synthesis process of GFS-MN. (b) Photographic images of MN mold and GFS-MN patch (scale bar: 0.5 cm). (c) SEM images of a GFS-MN patch (scale bars: 200 μm, 100 μm and 50 μm). (d) EDS elemental mapping of a GFS-MN patch (Fe, O, C elements; scale bar: 10 μm). (e) Mechanical properties of the GFS-MN patch. (f) HE staining image of the histological sections showing the transdermal MN (MN inserted into BALB/c mouse burn skin, scale bar: 100 μm).

3.3. Photothermal properties of GFe@SFMSs and GFS-MN

The black color of the as-obtained GFe@SFMSs implies that the material has potential photothermal properties. The relationship between the concentration of GFe@SFMSs and the photothermal effects under NIR laser irradiation (808 nm, 1.0 W cm^{-2}) was investigated. The temperature of the GFe@SFMSs suspension increased to 34.2, 35.4, 42.0, 49.8, 51.2, 51.6, and 53.6 °C at GFe@SFMSs concentrations of 0.25, 0.5, 1.0, 2.0, 4.0, 8.0, and 16.0 mg mL^{-1} ((Fig. 4b), demonstrating a concentration-dependent photothermal effect. Since temperatures above 50 °C can effectively inhibit bacteria, the concentration of the GFe@SFMSs loaded into the GFS-MN system was selected to be 4 mg mL^{-1}. In addition to material concentration, the effects of the laser power density on the photothermal heating ability of the GFe@SFMSs were also investigated. When the laser power density was increased to 0.5, 1, 1.5, and 2 W cm^{-2}, the temperature of the GFe@SFMSs suspension rose to 35.9, 41.3, 48.4, and 61.5 °C, respectively (Fig. S5, SI). In comparison, the temperature of GFS-MN reached 37.7, 56.7, 74.8, and 87.3 °C under the same conditions (Fig. 4d). Based on these results, a laser power density of 1.0 W cm^{-2} was selected as the optimal parameter for the antibacterial application of the GFS-MN and was used in all subsequent experiments. Under this parameter, the MN group exhibited almost no temperature change (a maximum of 23.7 °C, Fig. 4a and d), which is insufficient to kill bacteria.[24] In contrast, GFS-MN reached a temperature of 56.7 °C within 6 min, indicating its excellent photothermal performance (Fig. 4a and d). The on–off irradiation cycling experiment confirms that GFS-MN has outstanding photostability (Fig. 4e). Moreover, *in vivo* tests indicate that GFS-MN cam maintain the temperature above 55 °C—a level sufficient for effective bacterial eradication without causing significant harm to surrounding tissues (Fig. S6, SI).

3.4. *In vitro* antibacterial properties of GFS-MN

Burn wound surfaces are high-risk areas for bacterial infections, especially during the early stages of wound healing. Infection is one of the most common complications in the healing process of burn wounds, and in severe cases, it can lead to wound deterioration and even life-threatening conditions. The risk of infection in burn wounds increases over time. Early infections are primarily caused by Gram-positive bacteria, while in later stages, the wounds are more susceptible to infections by Gram-negative bacteria, which are more resistant to antibiotics.[41–43] This temporal shift in the pathogenic profile

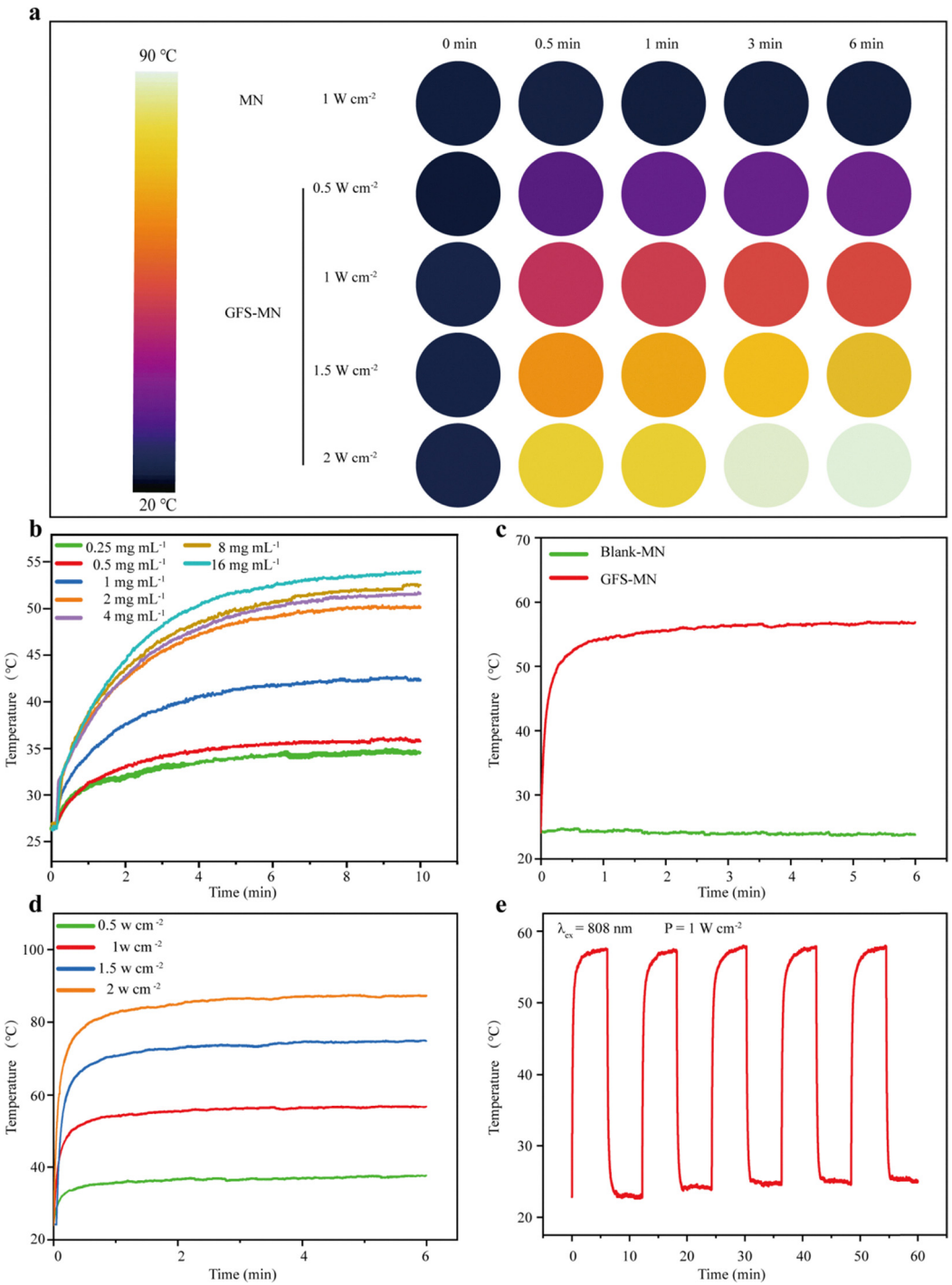

Fig. 4 The photothermal properties of the GFS-MN patch: (a) photothermal images of the MN and the GFS-MN with NIR irradiation (808 nm; MN: 1.0 W cm^{-2}, 6 min; GFS-MN: 0.5, 1.0, 1.5, 2.0 W cm^{-2}, 6 min). (b) Photothermal heating curves of GFe@SFMSs samples at different concentrations (0.25–16.0 mg mL^{-1}, NIR: 808 nm, 1.0 W cm^{-2}, 10 min). (c) Photothermal heating curves of GFS-MN under the 808 nm irradiation with different laser powers (808 nm, 0.5–2.0 W cm^{-2}, 10 min). (d) Photothermal heating curves of MN and GFS-MN under the NIR irradiation (808 nm, 1.0 W cm^{-2}, 6 min). (e) Photostability of GFS-MN (five ON/OFF cycles, NIR: 808 nm, 1.0 W cm^{-2}, 6 min per cycle).

imposes greater challenges and demands more sophisticated approaches in the treatment of burn wounds. Our GFS-MN dressing effectively addresses this issue through dual antibacterial mechanisms. During the early phase, it exerts potent antibacterial activity *via* the photothermal effect mediated by polyphenol-based small molecules and metal coordination bonds. In subsequent stages, it ensures prolonged antibacterial effects through the sustained release of antibacterial gallic acid and iron ions that inhibit bacteria *via* the Fenton reaction. Fig. 5a illustrates the dual antibacterial mechanisms of the

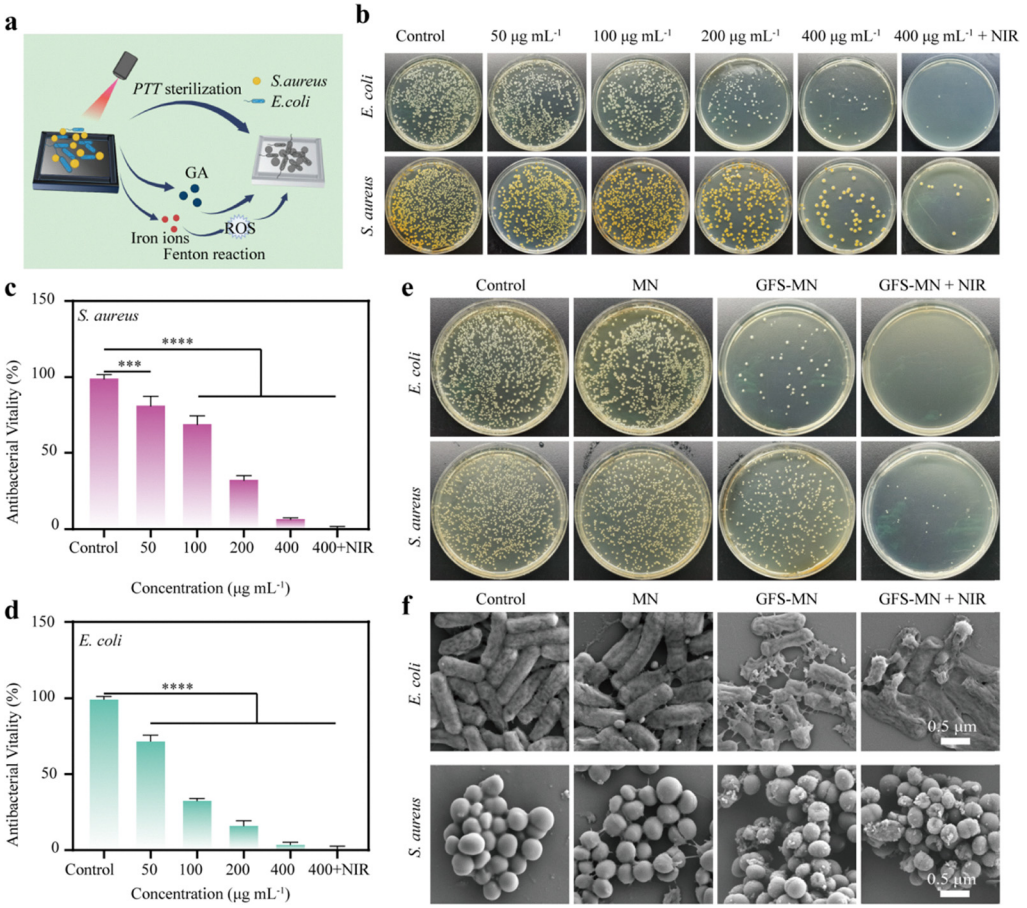

Fig. 5 Antibacterial Properties of GFe@SFMSs and GFS-MN *in vitro*: (a) schematic diagram of photothermal sterilization by GFS-MN. (b) Representative optical images of colony-forming units for *E. coli* and *S. aureus* suspensions co-cultured with different concentrations of GFe@SFMSs. (c) and (d) Corresponding quantitative analysis of bacterial colonies for *S. aureus* (c) and *E. coli* (d). (e) Representative optical images of colony-forming units of *E. coli* and *S. aureus* after co-cultivation with different groups. (f) Representative SEM images of *E. coli* and *S. aureus* colonies after co-cultivation with different groups (scale bar: 0.5 μm).

GFS-MN patch. The antibacterial performance of GFe@SFMSs was evaluated at a concentration of 400 μg mL^{-1}. The results show that GFe@SFMSs achieved inhibition rates of 96.7% against *E. coli* and 92.5% against *S. aureus*. Due to the photothermal conversion ability acquired after the coordination of gallic acid and iron ions, the antibacterial ability of the GFe@SFMSs can be further enhanced by combining photothermal sterilization. After combination with photothermal sterilization, the antibacterial efficacy against both *E. coli* and *S. aureus* exceeded 99% under NIR irradiation (Fig. 5b–d), indicating that GFe@SFMSs possess strong antibacterial capabilities to inhibit infections in burn wounds. Since GFe@SFMSs are loaded into microneedle patches for transdermal release, the antibacterial performance of GFS-MN was further assessed. Compared with the control group, the GFS-MN group showed significant inhibitory effects against bacteria, and the synergistic photothermal effects further enhanced the antibacterial ability of the GFS-MN patch (Fig. 5e).

To elucidate the potential antibacterial mechanisms, the morphological changes of bacteria co-cultured with different groups of samples were examined by SEM. In the control group, the three types of bacteria maintained their original morphology with smooth bacterial membranes. In contrast, bacteria co-cultured with GFS-MN and GFS-MN + NIR exhibited severe structural damage, characterized by extensive cell membrane rupture and perforation, which further corroborates its potent antibacterial efficacy. These results indicate that the combined sterilization approach resulted in markedly intensified bacterial destruction (Fig. 5f). Notably, the potentiated antibacterial efficacy of the GFS-MN patch under NIR irradiation is intrinsically coupled to the photothermally triggered structural and chemical remodeling of GFe@SFMSs. Specifically, NIR exposure induced controlled dissociation of the GA–Fe coordination network while preserving the spherical architectural integrity of GFe@SFMSs (Fig. S7a, SI). Concurrently, EDS revealed a moderate attenuation of Fe signal intensity post-photothermal treatment (Fig. S7b, SI), indicative of facilitated sustained release of bioactive gallic acid and Fe ions without compromising structural stability. More importantly, XPS analysis of the Fe 2p core-level spectrum (Fig. S7c, SI) demonstrated a pronounced redox transition of iron species following NIR irradiation, evidenced by a substantial increase in Fe^{2+} relative

abundance. This Fe^{2+} enrichment was attributed to accelerated ligand-to-metal charge transfer between GA and Fe^{3+} under photothermal stimulation, coupled with the hypoxic microenvironment of the silk fibroin matrix that suppressed re-oxidation of the generated Fe^{2+}. The enriched Fe^{2+} served as the catalytic center for Fenton reaction-mediated generation of highly $^{\bullet}OH$, inflicting damage to bacterial membranes and genomic DNA. This chemodynamic effect synergized with NIR-mediated photothermal ablation and GA-derived chemical antibacterial actions to elicit robust bactericidal activity against both Gram-positive and Gram-negative bacteria.

3.5. Cytotoxicity, proliferation, and migration of GFS-MN Patch

The cytocompatibility of the GFe@SFMSs was first evaluated using NIH/3T3 cells. The results show that the materials display negligible toxicity to cells at concentrations below 200 μg mL^{-1}, which demonstrates their good biocompatibility (Fig. 6a).

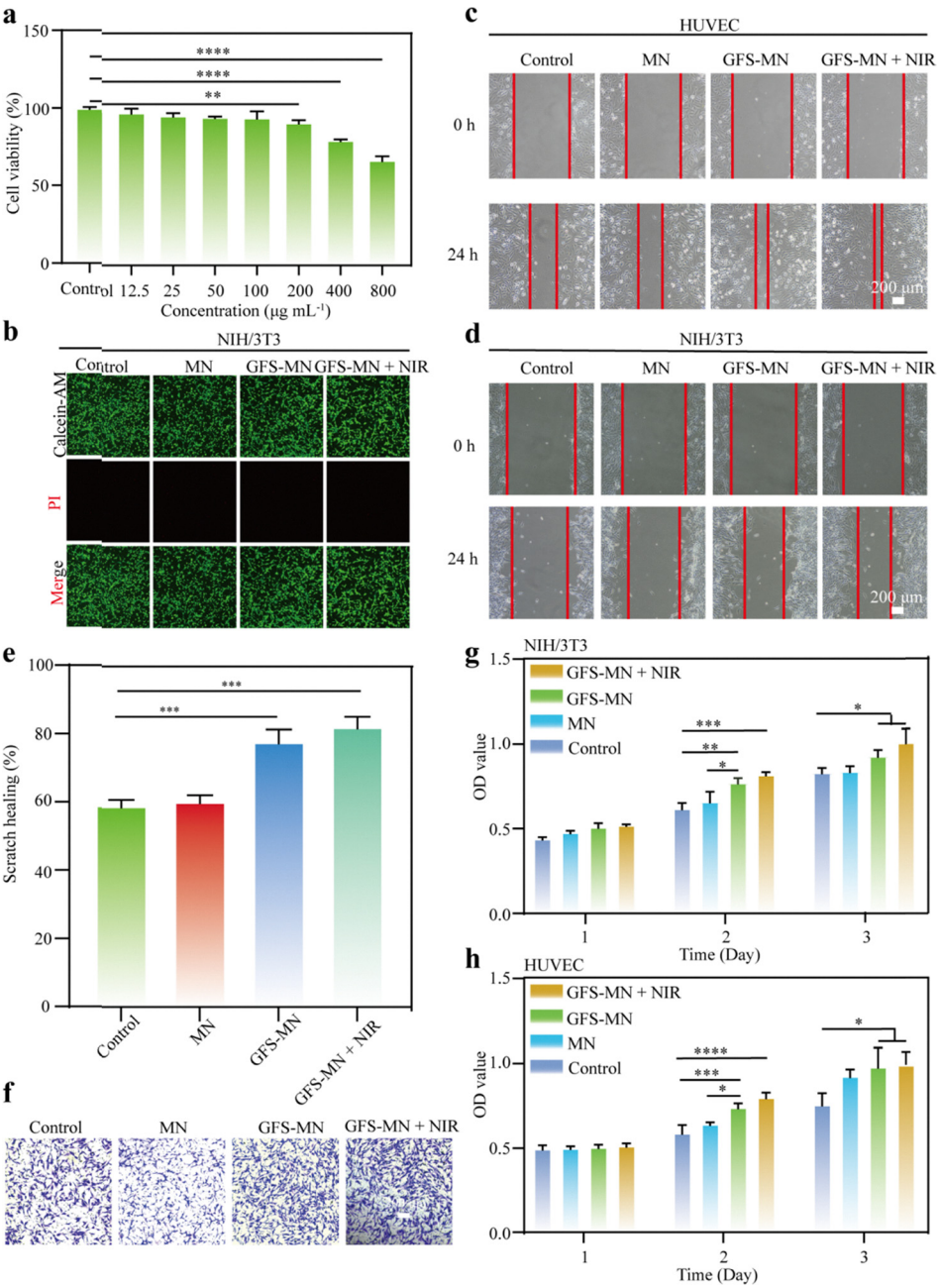

Fig. 6 *In vitro* biocompatibility of the GFS-MN: (a) cytotoxicity assessment of GFe@SFMSs at varying concentrations using NIH/3T3 cells. (b) Live/dead staining of NIH/3T3 treated with different groups. (c) and (d) Images of wound scratch healing assay for HUVEC (c) and NIH/3T3 (d) cells treated with different groups. (e) Quantification of HUVEC migration (n = 3). (f) Transwell assay staining results of NIH/3T3 cells in different groups. (g) and (h) Cell proliferation assay for different groups using NIH/3T3 (g) and HUVEC (h) cells. Data represent mean ± SD; *$p < 0.05$, **$p < 0.01$, ***$p < 0.001$.

The cytotoxicity of the MN was assessed using NIH/3T3 fibroblasts and HUVEC cells, and no significant differences were found across the experimental groups (Fig. S8, SI). Based on the results of preliminary experiments, a concentration of 200 μg mL^{-1} for GFe@SFMSs was chosen for the cell experiments. The blood compatibility of the GFS-MN was further evaluated. Fig. S9 demonstrates that the supernatant of the aqueous solution in the positive control group exhibited a distinct bright red color, indicating substantial hemolysis of red blood cells. In contrast, the supernatants from both the PBS and GFS-MN groups remained clear and colorless, with hemolysis rates measured below 5%. These results clearly show that the GFS-MN materials have excellent hemocompatibility, thus meeting a fundamental requirement for biomaterials used in tissue repair applications.

The biocompatibility of GFS-MN, both with and without NIR light irradiation, was evaluated using a live/dead cell staining assay. NIH/3T3 cells were incubated with the materials for 24 h. After the treatment, cell viability was evaluated using a Calcein-AM/PI double staining kit. The results show that the strong green fluorescence (indicating live cells) in the GFS-MN group was comparable to the control group. Only minimal red fluorescence (representing dead cells) was observed in both groups. These findings imply that GFS-MN has no significant cytotoxic effects on cell growth or survival, and that NIR irradiation did not cause any additional adverse responses under the tested conditions (Fig. 6b).

To further explore the effects of the GFS-MN patch on cell migration, an *in vitro* scratch assay was employed to evaluate the material's potential to promote wound healing. The scratch area of the control HUVEC cells remained nearly unchanged, indicating minimal cell movement towards the scratch (Fig. 6c). In contrast, HUVEC treated with GFS-MN displayed a significantly reduced remaining scratch area, accounting for only 22.0% of the original wound area. This was further decreased to 17.6% after NIR light stimulation ((Fig. 6e). These results suggest that active components within GFS-MN (*e.g.*, SF) potently promote HUVEC migration, an effect that can be enhanced by NIR irradiation. The synergistic enhancement of cell migration highlights the potential utility of GFS-MN, especially in combination with NIR stimulation, for wound healing applications. Scratch assays using NIH/3T3 cells and HSF (Human Skin Fibroblast) cells also reached similar conclusions (Fig. 6d and Fig. S10, SI). Additionally, a transwell assay was used to further verify its ability to promote cell migration *in vitro*. Compared with the control group, the GFS-MN and GFS-MN + NIR groups significantly enhanced the migration of NIH/3T3 cells (Fig. 6f). In the healing of burn infected wounds, the impaired function of endothelial cells and fibroblasts can delay the healing process. In this study, GFS-MN significantly promoted cell proliferation and migration through the bioactivity of silk fibroin.

In vitro experiments demonstrated that the GFS-MN group significantly promoted the proliferation of HUVEC and NIH/3T3 cells after 2 days and continued to accelerate cell proliferation within 3 days. Moreover, under NIR irradiation, the photothermal effect enhanced cell proliferation capacity (Fig. 6g and h), indicating that NIR treatment could further enhance the bioactivity of the system and accelerate cell growth.

3.6. Assessment of *in vitro* and *in vivo* antioxidant performance

In infected burn wounds, excessive reactive oxygen species (ROS) can trigger inflammatory responses, induce cell damage, and impede the tissue regeneration process. The free radical scavenging ability of GFS-MN primarily stems from the gallic acid (GA) in the GFe@SFMSs. To assess the free radical scavenging capacity of GFS-MN, two commonly used radical models, $ABTS^{+}$ and DPPH, were utilized. Both assays showed a concentration dependent scavenging effect of GFe@SFMSs samples after co-incubation. At a concentration of 200 μg mL^{-1}, GFe@SFMSs displayed scavenging rates of approximately 41.6% against $ABTS^{+}$ radicals and 54.2% against DPPH radicals (Fig. S11a–d, SI). These findings suggest that GFe@SFMSs possess remarkable free radical scavenging ability, which can effectively neutralize excessive ROS, thus inhibiting inflammatory responses, reducing cell damage, and creating favorable conditions for tissue regeneration in burn infected wounds.

Subsequently, the antioxidant capacity of GFS-MN was verified at the cellular level. A successful oxidative stress injury model was established *via* H_2O_2 treatment, as indicated by a significant increase in green fluorescence intensity. Initially, intracellular ROS levels were measured using the DCFH-DA fluorescent probe, which also enabled the investigation of the protective effects of GFS-MN under oxidative stress conditions. The results revealed that NIH/3T3 cells exposed to H_2O_2 showed significantly enhanced fluorescence intensity, indicating a substantial increase in intracellular ROS levels. In contrast, NIH/3T3 cells treated with GFS-MN extract exhibited a notable reduction in fluorescence intensity compared to the H_2O_2 treated group, suggesting efficient scavenging of intracellular ROS (Fig. S11e, SI). These results demonstrate GFS-MN's ability to alleviate oxidative stress by regulating cellular redox homeostasis, highlighting its potential therapeutic value in wound healing applications.

During the healing process of burn infected wounds, excessive ROS can activate inflammatory responses, induce cell damage, and impede tissue regeneration. Previously, we demonstrated the significant free radical scavenging ability of GFS-MN through *in vitro* experiments. Additionally, on day 7 post-treatment, *in vivo* ROS staining experiments were carried out. It was discovered that the fluorescence intensity of ROS in the wound tissues of the GFS-MN treated group was significantly lower than that of the control group treated with MN alone (Fig. S11f and g, SI). This result indicates that GFS-MN exhibits strong antioxidant capacity in the *in vivo* environment, outperforming simple MN treatment. This significant ROS scavenging effect is mainly due to the antioxidant properties of GA, a key component of GFS-MN, which can effectively neutralize excessive ROS, reduce oxidative stress damage, and inhibit inflammatory responses, thereby promoting the healing of burn infected wounds.

3.7. *In vivo* healing of burn wound infections

To evaluate the effects of GFS-MN on the healing of burn-infected wounds, a BALB/c mice burn infection model was established, and the rats were randomly divided into four groups: control group, blank microneedle group (MN group), GFS-MN treatment group, and GFS-MN combined with NIR irradiation group. Fig. 7a illustrates the construction of the infected full-thickness burn wound. Wound healing was assessed by sampling on day 14 after treatment. The results show that the wound areas in the GFS-MN treatment group and the GFS-MN combined with NIR irradiation group were smaller than those in the control and MN groups, with the most significant difference observed on day 10 (Fig. 7b and c). By day 10, the wounds in the GFS-MN + NIR group were nearly healed, indicating that the combination of GFS-MN and NIR irradiation substantially accelerated the healing process of burn-infected wounds. Histological observation *via* H&E staining revealed a significant reduction in inflammatory cell infiltration in both GFS-MN and the GFS-MN + NIR groups, with more evident formation of neoepithelium and granulation tissue. The most advanced tissue repair was evident in the GFS-MN combined with NIR irradiation group, where wound healing exhibited the highest degree of structural completeness (Fig. 7d). Masson's trichrome staining results show that the collagen deposition was greater in the GFS-MN and the GFS-MN + NIR groups than in the control and MN groups. The most substantial collagen deposition was observed in the GFS-MN + NIR group, indicating enhanced tissue repair under combined treatment (Fig. 7e). The superior tissue repair effects shown by the GFS-MN + NIR group is due to the synergistic antibacterial mechanism of the GFe@SFMSs under NIR light, as well as the anti-inflammatory effects of polyphenol small molecules and SF protein molecules released from the microspheres.

To further elucidate the mechanisms underlying tissue repair, immunofluorescence staining was conducted on samples collected on day 14 to assess the expression of multiple inflammatory factors. Immunofluorescence analysis indicated that both

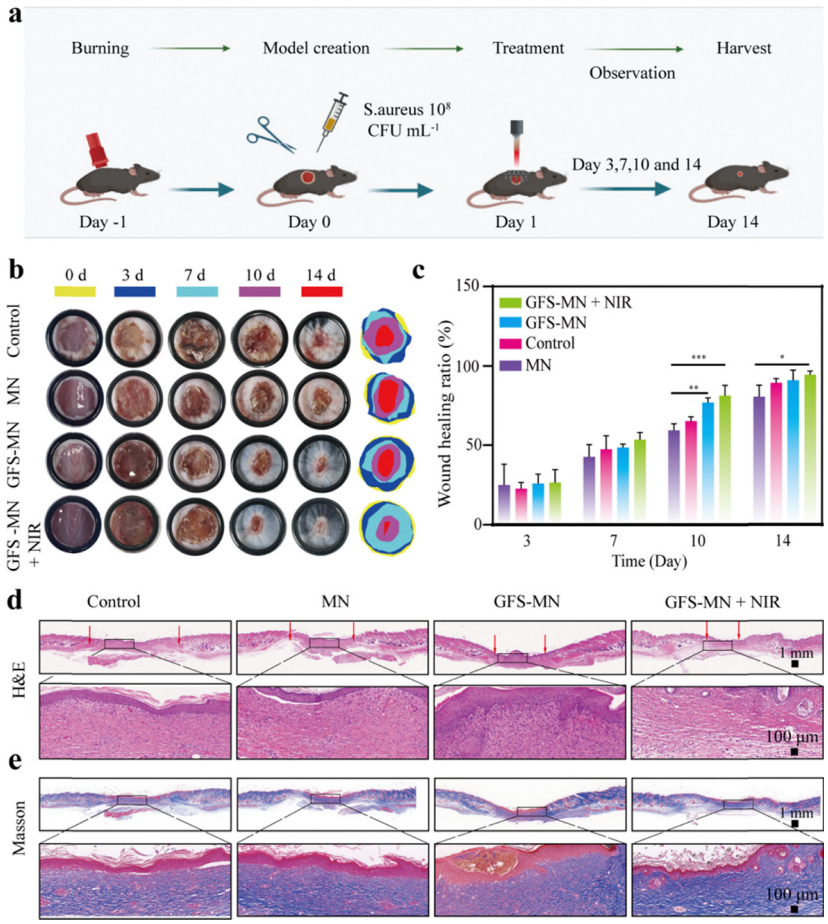

Fig. 7 *In vivo* evaluation of different MN in the treatment of infected burn wounds: (a) the timeline for constructing full-thickness skin wounds infected with pathogens and the wound healing process (BALB/c mice, 8 weeks old). (b) Representative images of the wound healing process in different groups. The internal diameter of the scale ring is 10 mm. Schematic diagram of the wound healed by different treatments during 14 days. (c) Quantitative data of relative wound area at different time points (n = 3). (d) Representative images of wound tissue sections in different groups stained by H&E on day 14 (scale bar: 1 mm and 100 μm). The dashed rectangular boxes show 10 times magnified images. The red arrows represent the granulation tissue gap. (e) Collagen deposition for different groups by Masson's trichrome staining. The dashed rectangular boxes show 10 times magnified images (scale bar: 1 mm and 100 μm).

the microvessel density (MVD), quantified by CD31 staining, and the number of α-SMA positive cells were significantly increased in the GFS-MN treatment group and the GFS-MN + NIR group compared with the control and MN only groups (Fig. 8a, b, f and g). These findings suggest that GFS-MN treatment significantly enhances angiogenesis and promotes vessel maturation, with a notably synergistic improvement observed upon NIR irradiation.

Additionally, the expression levels of inflammatory factors in the wound tissues were detected *via* immunofluorescence staining. Compared with the MN and control groups, the GFS-MN and GFS-MN + NIR groups showed a reduction in the fluorescence intensity of inflammatory factors (Fig. 8c, d, h and i). Although no significant differences were found in the expression levels of the pro-inflammatory factors TNF-α and IL-6 between the GFS-MN treatment group and the control or MN only groups, a remarkable reduction in both cytokines was detected in the GFS-MN + NIR group compared with the control and MN groups (Fig. 8h and i). This implies that the application of NIR irradiation may enhance the anti-inflammatory efficacy of GFS-MN, potentially through synergistic antibacterial and anti-inflammatory effects. Meanwhile, the expression level of the anti-inflammatory factor IL-10 was significantly higher in the GFS-MN + NIR group than in the control and MN groups (Fig. 8e and j). This suggests that the combined treatment of GFS-MN and NIR can effectively regulate the local inflammatory microenvironment, potentially by enhancing IL-10 mediated anti-inflammatory responses, thereby facilitating the wound healing process.

In the safety assessment, histological examination and biochemical marker detection revealed no significant pathological changes or toxic reactions in the heart, liver, spleen, lung, and kidney tissues of all four groups (*i.e.*, the control, MN, GFS-MN, and GFS-MN + NIR groups), indicating that GFS-MN and its combination with NIR irradiation had no significant toxicity to major organs under the experimental conditions (Fig. S12, SI). These results demonstrate that GFS-MN significantly promotes the healing of infected burn wounds through a synergistic mechanism that combines potent antibacterial activity, enhanced angiogenesis, and modulation of

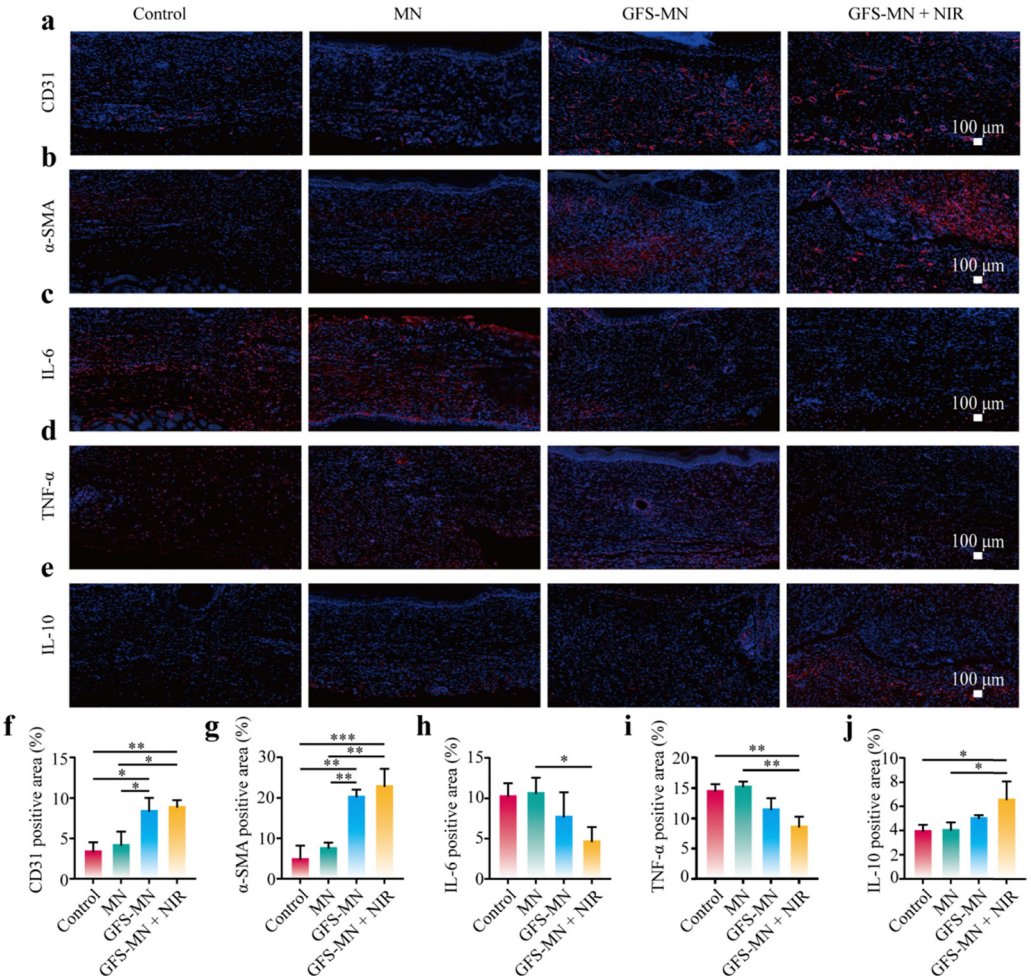

Fig. 8 Histological evaluation the assessment of anti-inflammation and angioblast: (a)–(e) Immunofluorescence staining images of CD31, α-SMA, IL-6, TNF-α, and IL-10 for different groups on day 14 (scale bar: 100 μm). (f)–(j) Quantitative analysis of the five indicators (CD31, α-SMA, IL-6, TNF-α, and IL-10) was performed across different groups. Data represent mean ± SD; $*p < 0.05$, $**p < 0.01$, $***p < 0.001$.

the inflammatory response—specifically by downregulating pro-inflammatory factors (TNF-α and IL-6) and upregulating the anti-inflammatory cytokine IL-10. Moreover, the treatment showed no significant toxicity in major organs, highlighting its potential as an effective and safe therapeutic strategy for burn infection management.

The GFS-MN patch simultaneously possesses antibacterial and anti-inflammatory effects through a coordinated multi-component mechanism. Its antibacterial effect relies on dual pathways: NIR irradiation-induced local heat (56.7 °C) directly ablates bacteria, and Fe ions released from the GFe network trigger Fenton reaction to generate ROS that damage bacterial membranes, while GA also exerts broad-spectrum antibacterial activity. For anti-inflammatory effects, GA scavenges excessive ROS (key pro-inflammatory inducers) in burn wounds, and SF degradation products polarize macrophages to the anti-inflammatory M2 phenotype, upregulating anti-inflammatory cytokines. Importantly, the two effects synergize: efficient bacterial clearance reduces bacterial-induced inflammation, and the anti-inflammatory effect creates a favorable microenvironment for bacterial clearance and tissue repair, as supported by experimental results showing >99% bacterial clearance and significant downregulation of pro-inflammatory cytokines in the GFS-MN + NIR group.

4. Conclusions

This study successfully developed a multifunctional microneedle (MN) patch system based on gallic acid–iron decorated silk fibroin microspheres (GFe@SFMSs) for the synergistic treatment of infected burn wounds. By fabricating a photothermally active metal–phenolic network on SFMSs and integrating them into silk fibroin-based microneedles, the resulting GFS-MN patch combines antibacterial, antioxidant, and anti-inflammatory functions in a spatially and temporally controlled manner. *In vitro* evaluations demonstrated that GFe@SFMSs exhibited strong antibacterial activity, achieving inhibition rates of 96.7% against *E. coli* and 92.5% against *S. aureus* at 400 μg mL^{-1}, with efficacy exceeding 99% under NIR irradiation. The patch also showed excellent biocompatibility, antioxidant capability, and promotive effects on cell proliferation and migration. *In vivo* studies using a burn-infected mouse model confirmed the therapeutic efficacy of GFS-MN, where NIR-assisted treatment significantly accelerated wound closure, reduced inflammatory infiltration, and enhanced regeneration of granulation tissue and epithelium. Mechanistically, the improved healing was correlated with an immunomodulatory shift, characterized by downregulation of pro-inflammatory cytokines (TNF-α and IL-6) and upregulation of anti-inflammatory IL-10. Collectively, the GFS-MN patch represents an effective and safe strategy for managing infected burn wounds through photothermal-chemicodynamic synergy and immunomodulation.

Conflicts of interest

The authors declare no conflicts of interest.

Data availability

The data supporting the findings of this study are included within the article and its supplementary information (SI), which contains processed experimental data, material characterization spectra (*e.g.*, SEM, FTIR, XPS), histological images, antibacterial efficacy results, photothermal performance curves, and statistical analysis summaries. See DOI: https://doi.org/10.1039/d6tb00149a.

Due to the nature of the experimental data (including proprietary experimental protocols and unprocessed raw data specific to the study), no external public data repository deposition has been conducted. However, all original datasets and experimental details required to reproduce the results are available from the corresponding author (Prof. Xinyu Zhao; Email: xyzhao@tongji.edu.cn) upon reasonable request, with appropriate institutional approval if necessary.

Acknowledgements

This research was supported by the National Key R&D Program of China (2022YFE0123500), the National Natural Science Foundation of China (32201102 and 52572298), the Shanghai Science and Technology Committee (BJKJ2024001), and the Science and Technology Bureau of Suzhou City (SZKJXM202318). We would like to express our sincere gratitude to Suzhou Pinglan Biotechnology Co., Ltd. for their support in terms of silk fibroin raw materials and processing technologies.

References

1 J. V. E. Gerstl, A. N. Ehsan, P. Lassarén, A. Yearley, N. P. Raykar, G. A. Anderson, T. R. Smith, S. R. Sabapathy and K. Ranganathan, *Plast. Reconstr. Surg.*, 2024, **153**, 743–752, DOI: 10.1097/prs.0000000000010595.
2 Y. Dong and Z. Wang, *Front. Bioeng. Biotechnol.*, 2023, **2023**, 112023, DOI: 10.3389/fbioe.2023.1304835.
3 M. A. Mofazzal Jahromi, P. Sahandi Zangabad, S. M. Moosavi Basri, K. Sahandi Zangabad, A. Ghamarypour, A. R. Aref, M. Karimi and M. R. Hamblin, *Adv. Drug Delivery Rev.*, 2018, **123**, 33–64.
4 J. Hu, Y. Lin, C. Cui, F. Zhang, T. Su, K. Guo and T. Chen, *Int. Wound J.*, 2023, **20**, 699–705.
5 M. E. Aljghami, S. Saboor and S. Amini-Nik, *Ann. Biomed. Eng.*, 2019, **47**, 659–675.
6 D. Chouhan, T.-U. Lohe, P. K. Samudrala and B. B. Mandal, *Adv. Healthcare Mater.*, 2018, **7**, e1801092.
7 M. Vidya and S. Rajagopal, *Int. J. Polym. Sci.*, 2021, **2021**, 9069924.
8 Y. Zhang, R. Sheng, J. Chen, H. Wang, Y. Zhu, Z. Cao, X. Zhao, Z. Wang, C. Liu, Z. Chen, P. Zhang, B. Kuang, H. Zheng, C. Shen, Q. Yao and W. Zhang, *Adv. Mater.*, 2023, **35**, 2210517.
9 Z. Tian, H. Chen and P. Zhao, *Front. Pharmacol.*, 2025, **16**, 1548837.

10 A. Aldahish, N. Shanmugasundaram, R. Vasudevan, T. Alqahtani, S. Alqahtani, A. Mohammad Asiri, P. Devanandan, T. Thamaraikani, C. Vellapandian and N. Jayasankar, *Pharmaceuticals*, 2024, **17**, 1305, DOI: 10.3390/ph17101305.
11 S. Indrakumar, T. K. Dash, V. Mishra, B. Tandon and K. Chatterjee, *ACS Polym. Au*, 2024, **4**, 168–188.
12 P. P. Patil, M. R. Reagan and R. A. Bohara, *Int. J. Biol. Macromol.*, 2020, **164**, 4613–4627.
13 S. Chen, Y. Xie, K. Ma, Z. Wei, X. Ran, X. Fu, C. Zhang and C. Zhao, *Bioact. Mater.*, 2024, **42**, 478–518.
14 R. Huang, J. Hu, W. Qian, L. Chen and D. Zhang, *Burns Trauma*, 2021, **9**, tkab026.
15 B. K. Utpal, B. Sutradhar, M. Zehravi, S. H. Sweilam, U. P. Panigrahy, D. Urs, A. F. Fatima, P. K. Nallasivan, G. S. Chhabra, M. Sayeed, M. A. Alshehri, S. O. Rab, S. L. Khan and T. B. Emran, *Naunyn-Schmiedeberg's Arch. Pharmacol.*, 2025, **398**, 2459–2485.
16 X. Wang, H. Li, F. Meng and L. Luo, *J. Mater. Chem. B*, 2021, **9**, 4710–4717.
17 Z. Sun, N. Cheng, Z. Cai, Z. Ying, H. Liu, Z. Chen, H. Zeng, M. Yin, H. Liu, S. Tan, X. Zhou, X. Zhao and F. Chen, *J. Mater. Sci. Technol.*, 2025, **219**, 158–172.
18 M. Yin, Z. Liu, Z. Sun, X. Qu, Z. Chen, Y. Diao, Y. Cheng, S. Shen, X. Wang, Z. Cai, B. Lu, S. Tan, Y. Wang, X. Zhao and F. Chen, *Adv. Sci.*, 2024, **11**, 2407251.
19 O. Cioanca, I.-I. Lungu, D. Batir-Marin, A. Lungu, G.-A. Marin, R. Huzum, A. Stefanache, N. Sekeroglu and M. Hancianu, *Pharmaceutics*, 2025, **17**, 194, DOI: 10.3390/pharmaceutics17020194.
20 T. Yao, X. Zeng, H. Li, T. Luo, X. Tao and H. Xu, *Int. J. Biol. Macromol.*, 2024, **269**, 132115.
21 L. Li, Z. Zhao, Y. Gao, X. Jiang, H. Liu, X. Guo, X. Huang, L. Zhou, C. Liu and X.-C. Shen, *ACS Appl. Mater. Interfaces*, 2025, **17**, 56017–56039.
22 W. Xu, Z. Lin, C. Cortez-Jugo, G. G. Qiao and F. Caruso, *Angew. Chem., Int. Ed.*, 2025, **64**, e202423654.
23 W. Chen, M. Liu, H. Yang, A. Nezamzadeh-Ejhieh, C. Lu, Y. Pan, J. Liu and Z. Bai, *Pharmaceutics*, 2023, **15**, 1323, DOI: 10.3390/pharmaceutics15051323.
24 J. Qin, N. Guo, J. Yang and Y. Chen, *Biosensors*, 2023, **13**, 776, DOI: 10.3390/bios13080776.
25 M. Cai, Y. Han, X. Zheng, B. Xue, X. Zhang, Z. Mahmut, Y. Wang, B. Dong, C. Zhang, D. Gao and J. Sun, *Materials*, 2024, **17**, 15, DOI: 10.3390/ma17010015.
26 I. R. Khalil, A. T. H. Burns, I. Radecka, M. Kowalczuk, T. Khalaf, G. Adamus, B. Johnston and M. P. Khechara, *Int. J. Mol. Sci.*, 2017, **18**, 313, DOI: 10.3390/ijms18020313.
27 I. E. Mba and E. I. Nweze, *World J. Microbiol. Biotechnol.*, 2021, **37**, 108.
28 P. Xu, C. Wen, C. Gao, H. Liu, Y. Li, X. Guo, X.-C. Shen and H. Liang, *ACS Nano*, 2024, **18**, 713–727.
29 A. A. Yaqoob, H. Ahmad, T. Parveen, A. Ahmad, M. Oves, I. M. I. Ismail, H. A. Qari, K. Umar and M. N. Mohamad Ibrahim, *Front. Chem.*, 2020, 8, DOI: 10.3389/fchem.2020.00341.
30 J. Chen, H. Niu, L. Guan, Z. Yang, Y. He, J. Zhao, C. Wu, Y. Wang, K. Lin and Y. Zhu, *Adv. Healthcare Mater.*, 2023, **12**, 2202474.
31 Y. Hou, X. Guo, J. Ran, X. Lu and C. Xie, *Bioact. Mater.*, 2025, **44**, 516–530.
32 T. Peng, Y. Chen, X. Luan, W. Hu, W. Wu, B. Guo, C. Lu, C. Wu and X. Pan, *Bioact. Mater.*, 2025, **45**, 274–300.
33 S. Jiang, J. Zhou, L. Wang, X. Liu, J. Sun, Y. Zhuang, L. Yu, H. Li, D. Li, Z. Zou, Z. Gao and K. Lin, *Interdiscip. Mater.*, 2025, **4**, 728–744.
34 D. Wang, J. Xing, Y. Zhang, Z. Guo, S. Deng, Z. Guan, B. He, R. Ma, X. Leng, K. Dong and Y. Dong, *Int. J. Nanomed.*, 2023, **18**, 6425–6448.
35 Y. R. Park, Md. T. Sultan, H. J. Park, J. M. Lee, H. W. Ju, O. J. Lee, D. J. Lee, D. L. Kaplan and C. H. Park, *Acta Biomater.*, 2018, **67**, 183–195.
36 A. Fernández-González, C. de Lorenzo González, S. Rodríguez-Varillas and R. Badía-Laíño, *Int. J. Biol. Macromol.*, 2024, **278**, 134834.
37 S. Ghalei and H. Handa, *Mater. Today Chem.*, 2022, **23**, 100673.
38 W. Sun, M. Yin, Z. Sun, H. Liu, J. Ru, F. Chen, H. Ni and X. Zhao, *Mater. Sci. Semicond. Process.*, 2025, **197**, 109689.
39 Q. Zhu, M. Jiang, Q. Liu, S. Yan, L. Feng, Y. Lan, G. Shan, W. Xue and R. Guo, *Biomater. Sci.*, 2018, **6**, 2472–2486.
40 Y. Du, Y. Huo, Q. Yang, Z. Han, L. Hou, B. Cui, K. Fan, Y. Qiu, Z. Chen, W. Huang, J. Lu, L. Cheng, W. Cai and L. Kang, *Exploration*, 2023, **3**, 20220041.
41 S. Zhou, S. Xiao, X. Wang, X. Wang and L. Han, *Antibiotics*, 2023, **12**, 1432, DOI: 10.3390/antibiotics12091432.
42 S. Roy, P. Mukherjee, S. Kundu, D. Majumder, V. Raychaudhuri and L. Choudhury, *Acute Crit. Care*, 2024, **39**, 214–225.
43 Y. Gong, Y. Peng, X. Luo, C. Zhang, Y. Shi, Y. Zhang, J. Deng, Y. Peng, G. Luo and H. Li, *Front. Cell. Infect. Microbiol.*, 2021, **11**, 681731, DOI: 10.3389/fcimb.2021.681731.

